Noise analysis of grating-based x-ray differential phase-contrast imaging with angular signal radiography*

Wali Faiz[1], Yuan Bao(鲍园)[2], Kun Gao(高昆)[1,†], Zhao Wu(吴朝)[1], Chen-Xi Wei(卫晨希)[1], Gui-Bin Zan(昝贵彬)[1], Pei-Ping Zhu(朱佩平)[3,‡], and Yang-Chao Tian(田扬超)[1,§]

[1] *National Synchrotron Radiation Laboratory, University of Science and Technology of China, Hefei* 230029, *China*
[2] *Shanghai United Imaging Healthcare Co. Ltd., Shanghai* 201807, *China*
[3] *Institute of High Energy Physics, Chinese Academy of Sciences, Beijing* 100049, *China*

(Received 17 November 2016; revised manuscript received 6 January 2017; published online 10 March 2017)

X-ray phase-contrast imaging is one of the novel techniques, and has potential to enhance image quality and provide the details of inner structures nondestructively. In this work, we investigate quantitatively signal-to-noise ratio (SNR) of grating-based x-ray phase contrast imaging (GBPCI) system by employing angular signal radiography (ASR). Moreover, photon statistics and mechanical error that is a major source of noise are investigated in detail. Results show the dependence of SNR on the system parameters and the effects on the extracted absorption, refraction and scattering images. Our conclusions can be used to optimize the system design for upcoming practical applications in the areas such as material science and biomedical imaging.

Keywords: angular signal radiography, signal-to-noise ratio, photon statistical noise, mechanical error

PACS: 06.30.Bp, 43.60.Cg, 42.50.Wk, 37.10.Vz **DOI:** 10.1088/1674-1056/26/4/040602

1. Introduction

X-rays have been utilized to probe inner structures nondestructively since its discovery by Wilhelm Röntgen in 1895. Attenuation-contrast x-ray imaging, based on absorption of x-rays in the sample has been extensively used in nondestructive testing, biomedical imaging and security screening. However, the contrast produced due to difference in attenuation of x-rays is limited when weak-absorbing materials are imaged. In other words, low Z (proton number) elements, organic materials and body soft tissues are hard to image by attenuation-contrast x-ray imaging. Fortunately, this difficulty of low absorption contrast of soft tissue can be overcome with phase-contrast imaging.[1,2]

During the past two decades, the x-ray phase contrast imaging has received attention because x-ray phase shift cross section is much larger than the cross section of absorption.[1] X-ray phase contrast imaging attained extremely high sensitivity to weakly absorbing objects.[2] There are several x-ray phase sensitive imaging methods including: interferometric imaging,[3,4] analyzer-based imaging (ABI),[5–8] and propagation-based imaging (PBI).[9,10] Compared with other methods mentioned above, the grating interferometry has gained much attention as it is compatible with both synchrotron source and laboratory x-ray source.[11] Grating interferometer has good absorption and phase sensitivity, and its resolution is on the order of tens of microns.[12] Therefore, grating-based phase contrast imaging (GBPCI) has the potential to have medical applications as well as other image processing applications.

Since the demonstration of x-ray grating interferometry,[13,14] GBPCI has received much attention in medical imaging field.[15–19] In 2005, Weitkamp *et al.*[20] used the grating interferometry as a phase contrast imaging technique. After that, a breakthrough came into being in the field of x-ray phase contrast imaging so called Talbot-Lau interferometry.[11,21] In 2008, dark-field image concept was added to x-ray grating interferometery.[12] In order to limit radiation dose, the extraction methods are very important. In x-ray phase-contrast imaging, several extraction methods have been established in order to separate absorption, refraction and scattering signals from the projection image. Phase-stepping (PS) is the most widely used technique to extract information; however, its discontinuous image acquisition mode impairs wide clinical applications. In 2010, Zhu *et al.*[22] proposed a reverse projection (RP) method, which is fast, simple and low dose. In 2011–2012, Zanette *et al.*[23] introduced interlaced and sliding window phase-stepping[24] extraction techniques in order to lessen dose in phase contrast tomography. Recently, Li *et al.*[25] proposed an extraction method for grating interferometry, so-called angular signal radiography (ASR) which reduces

*Project supported by the National Natural Science Foundation of China (Grant Nos. 11535015, 11305173, and 11375225).
†Corresponding author. E-mail: gaokun@ustc.edu.cn
‡Corresponding author. E-mail: zhupp@ihep.ac.cn
§Corresponding author. E-mail: ychtian@ustc.edu.cn
© 2017 Chinese Physical Society and IOP Publishing Ltd

over all radiation doses and improves image acquisition speed.

Noise property is one of the important characteristics of the imaging system. Hence, many research groups[26–28] analyzed the noise for PS method. In 2014, Wu *et al.*[29] proposed the quantitative analysis of signal-to-noise ratios (SNRs) for RP method. However, RP method can extract absorption and refraction information only. ASR can extract absorption, refraction, and scattering as well. In this regard, we propose SNRs quantitative analysis of images acquired by ASR method for GBPCI. Two main causes of noise photon fluctuations and mechanical error are investigated by using the error propagation formula.[30] Theoretical expressions of SNRs of absorption, refraction and scattering images of ASR method are obtained. The results show how several parameters of the imaging system affect the noise of GBPCI and how the image quality can be improved.

2. Principle of angular signal radiography

The schematic setup of Talbot interferometer is shown in Fig. 1(a). It is comprised of an x-ray source, a rotary sample station, a phase grating G1 (period p_1), an analyzer grating G2 (period p_2), and a detector. G1 and G2 are positioned in a straight line in front of the detector. The G1 functions as a splitter or an angular collimator while G2 acts as an angular filter. In the case of grating interferometer, G2 is set at self-image distance (D) behind G1. The photon number at the detector changes when G2 is moved by small displacement x_g with respect to G1 in the orthogonal direction of the x-ray beam and the grating line. Generally, we refer to the curve of intensity vs. grating relative position as shifting curve (SC), and the normalized SC of x-ray grating interferometer (XGI) is shown in Fig. 1(b). In XGI setup, the displacement x_g between G1 and G2 is equivalent to angular deviation (x_g/D) induced by the sample. Different points on SC corresponding to valley-SC, upslope-SC, peak-SC, and downslope-SC are marked as V, U, P, and D respectively (shown in Fig. 1(b)). Hence, angular signal response function (ASRF) is given as[25]

$$S(\psi) = S(x_g/D) = \overline{S}\left[1 - V_0 \cos\left(\frac{2\pi D}{p_2}(\psi + \psi_0) + \eta\frac{\pi}{2}\right)\right], \quad (1)$$

where $\overline{S} = (S_{\max} + S_{\min})/2$, the average value; $V_0 = (S_{\max} - S_{\min})/(S_{\max} + S_{\min})$, visibility; $S_{\max}$ and $S_{\min}$ are maximum and minimum value of normalized SC respectively; ψ_0 and ψ are the initial x-ray deviation angle and x-ray deviation angle respectively; $\eta = 0, 1, 2, 3$ are the modulation parameters to obtain four SCs.

By considering the absorption, refraction and scattering interaction of x-rays with object, the angle modulated function (AMF) can be depicted as[31]

$$f(\psi;x,y) = I_0 \frac{\exp(-M(x,y))}{\sqrt{2\pi}\vartheta(x,y)} \exp\left[-\frac{1}{2}\frac{(\psi - \theta(x,y))^2}{\vartheta^2(x,y)}\right], \quad (2)$$

where I_0 is the incident total photon number of x-ray beam, $M(x,y) = \int_{-\infty}^{\infty} \mu(x,y,z)\,\mathrm{d}z$ the absorption of sample, $\mu(x,y,z)$ the absorption coefficient,

$$\theta(x,y) = -\int_{-\infty}^{\infty} \frac{\partial \delta(x,y,z)}{\partial x}\,\mathrm{d}z$$

the refraction angle induced by sample, $\delta(x,y,z)$ the decrement of real part of refractive index, and $\upsilon^2(x,y) = \int_{-\infty}^{\infty} \omega(x,y,z)\,\mathrm{d}z$ the scattering variance, and $\omega(x,y,z)$ being scattering coefficient. The intensity detected by the detector is deformed by the absorption, refraction and scattering produced by sample placed in the x-ray beam before or after G1. Hence, by ASR[25] in XGI, the detected image function $I(\psi;x,y)$ can be obtained by taking the convolution of AMF and ASRF.

$$I(\psi;x,y) = f(\psi;x,y) \otimes S(\psi), \quad (3)$$

where $\otimes$ represents convolution.

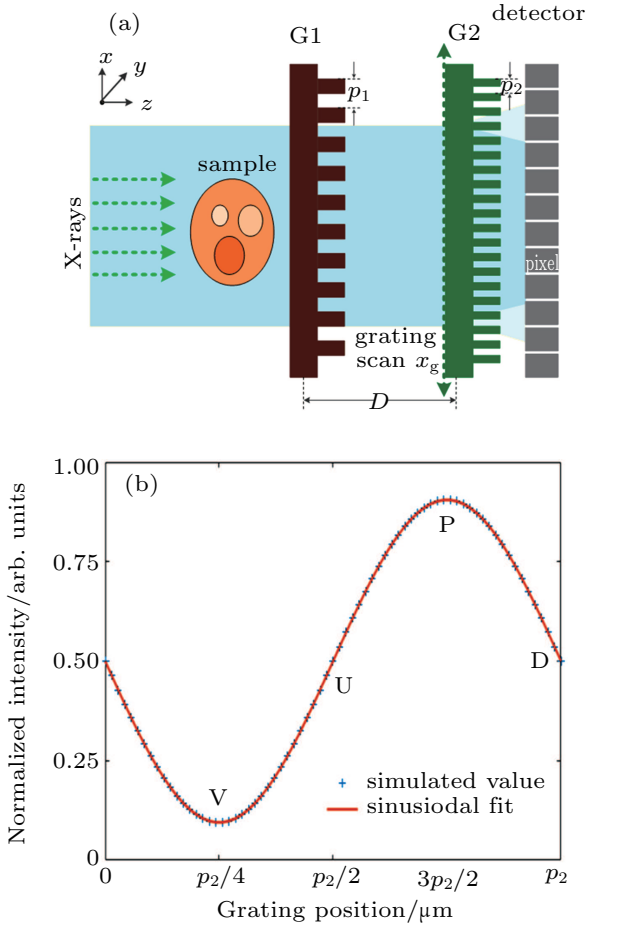


Fig. 1. (color online) Schematic setup of GBPCI. (a) Periodic interference pattern of G1 is formed in the plane of G2 through Talbot self-imaging; (b) plot of shifting curve as a function of the grating position for detector pixel over one period of G2.

By substituting Eqs. (1) and (2) into Eq. (3) we obtain the expressions of valley-image ($I_{\rm V}$), upslope-image ($I_{\rm U}$), peak-image ($I_{\rm P}$), and downslope-image ($I_{\rm D}$) in the following expressions:[25]

$$I_{\rm V}(x,y) = I_0\bar{S}\,{\rm e}^{-M(x,y)}\left[1 - V(x,y)\cos\varphi(x,y)\right], \quad (4)$$

$$I_{\rm U}(x,y) = I_0\bar{S}\,{\rm e}^{-M(x,y)}\left[1 + V(x,y)\sin\varphi(x,y)\right], \quad (5)$$

$$I_{\rm P}(x,y) = I_0\bar{S}\,{\rm e}^{-M(x,y)}\left[1 + V(x,y)\cos\varphi(x,y)\right], \quad (6)$$

$$I_{\rm D}(x,y) = I_0\bar{S}\,{\rm e}^{-M(x,y)}\left[1 - V(x,y)\sin(\varphi(x,y))\right], \quad (7)$$

where

$$V(x,y) = V_0\,{\rm e}^{-2\pi^2D^2\vartheta^2(x,y)/p_2^2},$$

$$\varphi(x,y) = \frac{2\pi D}{p_2}\left(\theta(x,y) + \psi_0\right).$$

Now by combining Eq. (4) to Eq. (7) the absorption, refraction and scattering information can be deduced and simplified as

$$M(x,y) = -\ln\left[\frac{I_{\rm U}(x,y) + I_{\rm D}(x,y)}{2I_0\bar{S}}\right], \quad (8)$$

$$\theta(x,y) = -\frac{p_2}{2\pi D}\arctan\left[\frac{I_{\rm U}(x,y) - I_{\rm D}(x,y)}{I_{\rm U}(x,y) + I_{\rm D}(x,y) - 2I_{\rm P}(x,y)}\right] - \psi_0, \quad (9)$$

$$\vartheta^2(x,y) = -\frac{p_2^2}{2\pi^2D^2}\ln\left[\frac{\sqrt{\left(I_{\rm U}(x,y) - I_{\rm D}(x,y)\right)^2 + \left(I_{\rm U}(x,y) + I_{\rm D}(x,y) - 2I_{\rm P}(x,y)\right)^2}}{V_0\left(I_{\rm U}(x,y) + I_{\rm D}(x,y)\right)}\right], \quad (10)$$

where $I_{\rm V}(x,y) = I_{\rm U}(x,y) + I_{\rm D}(x,y) - I_{\rm P}(x,y)$.

3. Noise analysis

Photon statistical noise and mechanical error are the two major factors affecting extraction information and image quality. SNRs analyses of GBPCI with reverse projection (RP) method of absorption and refraction images have been performed.[29] Here, the effects of photon statistics and mechanical error on the noise properties of absorption, refraction and scattering signals retrieved by ASR are discussed.

3.1. Photon statistical noise

The absorption coefficient, refraction angle and scattering variance fluctuate about a mean value ($a = \bar{a} + \Delta a$) because of the statistical fluctuations of the photon number. We suppose that the photon number follows Poisson statistics ($\sigma_{I_i}^2 = \bar{I}_i$), by using the error propagation formula,[30] the noise variances of absorption, refraction and scattering images are calculated by the noise variance of the measurement taken at each pixel position of the x-ray grating interferometer. After mathematical calculations (the detailed derivation is presented in Appendix A), the simplified expressions of SNRs due to photon statistics of absorption, refraction and scattering images are given as follows (for simplicity we drop (x,y)):

$${\rm SNR}_{M,{\rm st}} = \sqrt{2I_0\bar{S}\,{\rm e}^{-M}}\bar{M}, \quad (11)$$

$${\rm SNR}_{\theta,{\rm st}} = \frac{2\sqrt{2}\pi D}{p_2}\frac{\sqrt{I_0\bar{S}\,{\rm e}^{-M}}\bar{\theta}V}{\sqrt{1 + 2(1 + 2V\cos\varphi)\sin^2\varphi}}, \quad (12)$$

$${\rm SNR}_{\vartheta^2,{\rm st}} = \frac{2\sqrt{2}\pi^2D^2}{p_2^2} \times \frac{\sqrt{I_0\bar{S}\,{\rm e}^{-M}}\bar{\vartheta}^2V}{\sqrt{1 - V^2 + 4V\cos^3\varphi + 2\cos^2\varphi(1 + V^2)}}, \quad (13)$$

where ${\rm SNR}_{M,{\rm st}}$,${\rm SNR}_{\theta,{\rm st}}$, and ${\rm SNR}_{\vartheta^2,{\rm st}}$ are SNRs due to photon statistics of absorption, refraction, and scattering images respectively. Here, we point out that the SNRs of absorption, refraction, and scattering images are directly proportional to the square root of the incident photon number and also depends on sample absorption property. The SNRs of all the three images are proportional to square root of the mean value of background SC. Moreover, the SNR of absorption image is independent of reduced visibility (V) of SC, while the SNRs of refraction and scattering images depend on V. In addition, the SNRs of refraction and scattering images depend on phase shift (φ). Further, the SNR of absorption image is independent of system parameters, while SNRs of refraction and scattering images depend on system parameters like p_2 and D.

3.2. Mechanical error

The phase stepping is generally performed by translating G2 (or G1). But due to mechanical error the actual position ($x_{\rm g}$) about the ideal position can be depicted by a normal distribution with standard deviation $\sigma_{x_{\rm g}}$. In XGI, considering the mechanical error the photon number detected by the detector can be expressed as[25];

$$I(x,y) = I_0\bar{S}\,{\rm e}^{-M}\left[1 - V\cos\left(\varphi + \frac{2\pi}{p_2}x_{\rm g}\right)\right], \quad (14)$$

using error propagation formula,[30] and after mathematical calculations (the detailed derivation is presented in Appendix B), the simplified expressions of SNRs due to mechanical error of absorption, refraction and scattering images are given as follows:

$${\rm SNR}_{M,{\rm me}} = \frac{1}{\sqrt{2}\pi}\frac{p_2}{V\cos\varphi}\frac{\bar{M}}{\sigma_{x_{\rm g}}}, \quad (15)$$

$$\mathrm{SNR}_{\theta,\mathrm{me}} = \frac{\sqrt{2}D\bar{\theta}}{\sqrt{\cos^2\varphi + 2\sin^4\varphi}} \frac{1}{\sigma_{x_\mathrm{g}}}, \tag{16}$$

$$\mathrm{SNR}_{\vartheta_s^2,\mathrm{me}} = \frac{\sqrt{2}\pi D^2\bar{\vartheta}^2}{p_2\cos\varphi\sqrt{3+V^2+2\cos\varphi(V-\cos\varphi)}} \frac{1}{\sigma_{x_\mathrm{g}}}, \tag{17}$$

where $\mathrm{SNR}_{M,\mathrm{me}}$, $\mathrm{SNR}_{\theta,\mathrm{me}}$, and $\mathrm{SNR}_{\vartheta^2,\mathrm{me}}$ are the SNRs for absorption, refraction, and scattering images due to mechanical error, in which, we highlight that the SNRs of absorption, refraction, and scattering images are inversely proportional to σ_{x_g} and independent of I_0. Furthermore, the SNRs of absorption and scattering images depend upon p_2 but in different ways, while SNRs of refraction and scattering images depend on D. We also point out that due to mechanical error, the SNR of refraction image does not depend on V while those of absorption and scattering images depend on V.

4. Simulation and discussion

The predictions of the theoretical derivations of noise analysis for GBPCI are verified by performing simulation using Matlab. In simulations, Talbot interferometer is operated with plane-wave x-ray beam of 25 keV ($\lambda = 0.049$ nm). Talbot interferometer is comprised of G1 ($\pi/2$ phase shift) and G2 having periods $p_1 = p_2 = 4$ μm. A CCD detector of 10 μm×10 μm pixel size is used. The distance from G1 to G2 is set to be 16.13 cm. A cylindrical polymethyl methacrylate (PMMA) having 4-mm diameter is selected as a sample. The size of spherical scattering particles is 0.5 μm. The complex refractive index is $n = 1 - 4.26\times10^{-7} + \mathrm{i}1.53\times10^{-10}$ at 25 keV. To verify the expressions in Eqs. (11)–(13), , the SNRs due to photon noise are simulated for different incident x-ray intensities and repeated 10^4 times to compute variances. That is why the results are statistically significant. Similarly, the expressions in Eqs. (15)–(17), the SNRs due to mechanical error are simulated for different values of relative standard deviation $(\sigma_{x_\mathrm{g}}/p_2)$ of different stepping motors having precision of 0.0012, 0.0014, 0.0016, 0.0018, 0.0020, 0.0022, and 0.0024 while incident photon number is fixed at 5000 photon per pixel.

Figure 2 shows simulated SNRs as a function of incident photon number as well as theoretical predictions of SNRs due to photon statistics. Good agreement is observed between simulation and theoretical model. According to theoretical model, the SNRs due to photon statistics of absorption, refraction and scattering images are directly proportional to square root of I_0. Furthermore, the SNR of absorption image is independent of refraction angle while SNRs of scattering and refraction images depend on refraction angle. Here, we point out that SNR of refraction image is higher than those of absorption and scattering image, the reason is that SNRs are calculated near the edge of the sample. The simulated SNRs due to mechanical error and theoretical predictions are shown in Fig. 3. It is observed that simulated and theoretical predictions are well matched. Figure 3 shows that the SNRs of all the three images are inversely proportional to standard deviation.

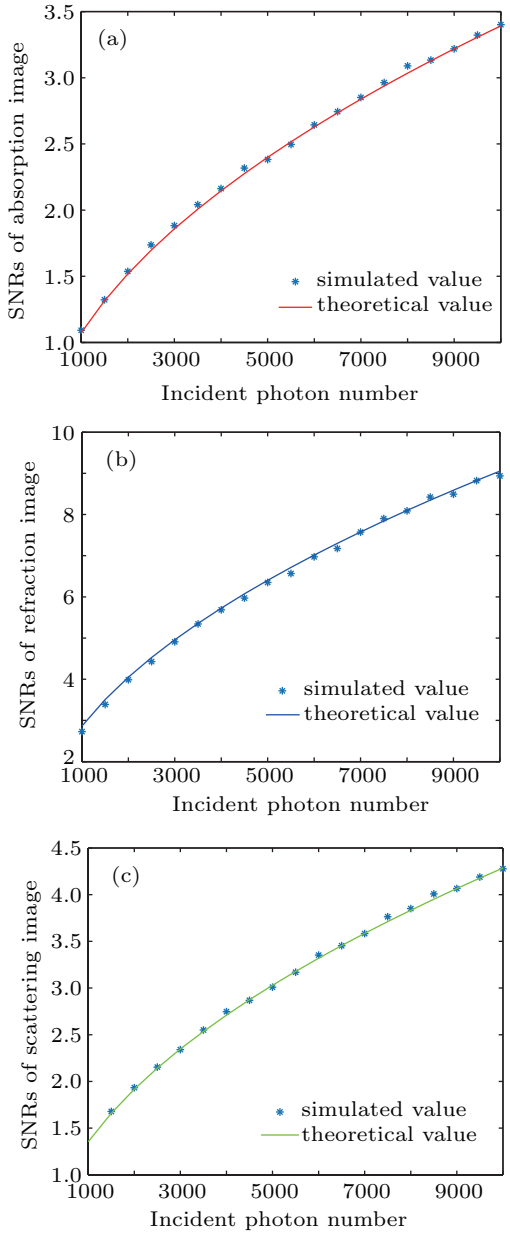


Fig. 2. (color online) The SNRs due to photon statistics versus incident photon number: absorption (a), refraction (b), and scattering (c) images.

Other noise sources, like electronic noise of CCD detector and fixed pattern noise, though have negligible effect, but reduce image quality. Electronic noise of CCD detector called dark current can be measured by obtaining an image while x-ray source is switched off. Fixed pattern noise caused by spatial non-uniformities of grating and/or detector and by mechanical drift of one grating with respect to other can produce artifacts in the image. In order to minimize these noises, temperature control, optimized mechanical design and gain correction can be implemented.

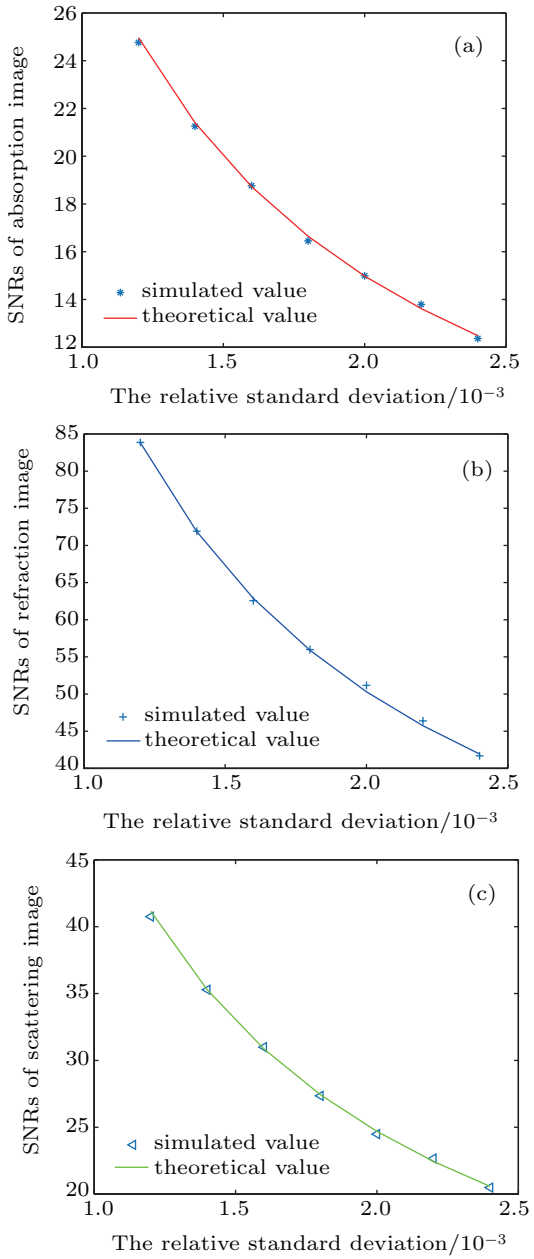


Fig. 3. (color online) The SNRs due to mechanical error versus relative standard deviation for absorption (a), refraction (b), and scattering (c) images.

5. Conclusions

In this work, we develop and analyze quantitatively SNRs of absorption, refraction, and scattering images of GBPCI by using Talbot interferometer employing ASR. Two main sources of noise, photon statistics and mechanical error are investigated in detail. The theoretical predictions developed in Section 3 are verified by performing simulations. All simulation and theoretical results show good agreement and hence validates our theoretical model. In the case of photon statistical noise, SNRs of all three images are directly proportional to square root of I_0, while due to mechanical noise, SNRs of all three images are inversely proportional to relative standard deviation. In addition, the dependence of other factors on SNRs of all three images is also discussed. Two approaches may be considered to improve the quality of extracted images: by increasing incident photon number and by using high-precision control system to reduce mechanical error. Finally, the image quality of refraction and scattering information can be enhanced by using the optimized inter-grating distance. However, x-ray tubes are power limited, so trade-off must be considered between image quality and measurement time. Finally, our results can be used to find optimized configuration to achieve better image quality.

Acknowledgment

The author, Wali Faiz, wishes to thank the Chinese Academy of Sciences and The World Academy of Sciences (CAS-TWAS) President's Fellowship Program for financial support.

Appendix A: Derivation of $\sigma_{M,\mathrm{st}}$, $\sigma_{\theta,\mathrm{st}}$, and $\sigma_{\upsilon^2,\mathrm{st}}$

The standard deviations of absorption, refraction, and scattering due to photon statistics are derived as

$$\sigma^2_{M,\mathrm{st}} = \sum_{i=\mathrm{U,D}} \left(\frac{\partial M}{\partial I_i}\right)^2_{I_i=\bar{I}_i} \sigma^2_{I_i} = \frac{1}{\bar{I}_\mathrm{U}+\bar{I}_\mathrm{D}}.$$

Using Eqs. (5) and (7), we obtain

$$\sigma^2_{M,\mathrm{st}} = \frac{1}{2I_0\bar{S}\mathrm{e}^{-M}},$$
$$\sigma^2_{\theta,\mathrm{st}} = \sum_{i=\mathrm{U,P,D}} \left(\frac{\partial \theta}{\partial I_i}\right)^2_{I_i=\bar{I}_i} \sigma^2_{I_i}. \tag{A1}$$

Using Eq. (9), we have

$$\sigma^2_{\theta,\mathrm{st}} = \left(\frac{p_2^2}{\pi^2 D^2}\right) \frac{\left(\bar{I}_\mathrm{D}-\bar{I}_\mathrm{P}\right)^2\bar{I}_\mathrm{U} + \left(\bar{I}_\mathrm{U}-\bar{I}_\mathrm{D}\right)^2\bar{I}_\mathrm{P} + \left(\bar{I}_\mathrm{P}-\bar{I}_\mathrm{U}\right)^2\bar{I}_\mathrm{D}}{\left[\left(\bar{I}_\mathrm{U}+\bar{I}_\mathrm{D}-2\bar{I}_\mathrm{P}\right)^2 + \left(\bar{I}_\mathrm{U}-\bar{I}_\mathrm{D}\right)^2\right]^2}.$$

Substituting Eqs. (5)–(7) into the above equation, we have

$$\sigma^2_{\theta,\mathrm{st}} = \left(\frac{p_2^2}{\pi^2 D^2}\right) \frac{1+2\left(1+2V\cos\varphi\right)\sin^2\varphi}{8I_0V^2\bar{S}\mathrm{e}^{-M}},$$
$$\sigma^2_{\upsilon^2,\mathrm{st}} = \sum_{i=\mathrm{U,P,D}} \left(\frac{\partial \upsilon^2}{\partial I_i}\right)^2_{I_i=\bar{I}_i} \sigma^2_{I_i}. \tag{A2}$$

Using Eq. (10), we have

$$\begin{aligned}\sigma^2_{\upsilon^2,\mathrm{st}} = {} & \left(\frac{p_2^2}{\pi^2 D^2}\right)^2 \frac{1}{\left[\left(\bar{I}_\mathrm{U}+\bar{I}_\mathrm{D}-2\bar{I}_\mathrm{P}\right)^2 + \left(\bar{I}_\mathrm{U}-\bar{I}_\mathrm{D}\right)^2\right]^2} \\ & \times \left[\frac{\left(\bar{I}_\mathrm{U}\bar{I}_\mathrm{D}+\bar{I}_\mathrm{U}\bar{I}_\mathrm{P}+\bar{I}_\mathrm{P}\bar{I}_\mathrm{D}-\bar{I}_\mathrm{D}^2-2\bar{I}_\mathrm{P}^2\right)^2}{\left(\bar{I}_\mathrm{U}+\bar{I}_\mathrm{D}\right)^2}\bar{I}_\mathrm{U}\right. \\ & + \left(\bar{I}_\mathrm{U}+\bar{I}_\mathrm{D}-2\bar{I}_\mathrm{P}\right)^2\bar{I}_\mathrm{P} \\ & \left. + \frac{\left(\bar{I}_\mathrm{U}\bar{I}_\mathrm{D}+\bar{I}_\mathrm{U}\bar{I}_\mathrm{P}+\bar{I}_\mathrm{P}\bar{I}_\mathrm{D}-\bar{I}_\mathrm{U}^2-2\bar{I}_\mathrm{P}^2\right)^2}{\left(\bar{I}_\mathrm{U}+\bar{I}_\mathrm{D}\right)^2}\bar{I}_\mathrm{D}\right].\end{aligned}$$

Substituting Eqs. (5)–(7) into the above equation, we have

$$\sigma^2_{\upsilon^2,\mathrm{st}} = \left(\frac{p_2^2}{\pi^2 D^2}\right)^2 \frac{1-V^2+4V\cos^3\varphi+2\cos^2\varphi(1+V^2)}{8I_0V^2\bar{S}\mathrm{e}^{-M}}. \tag{A3}$$

Appendix B: Derivation of $\sigma_{M,\mathrm{me}}$, $\sigma_{\theta,\mathrm{me}}$, and $\sigma_{\upsilon^2,\mathrm{me}}$

The standard deviations due to mechanical error are derived as

$$\sigma^2_{M,\mathrm{me}} = \left[\left(\frac{\partial M}{\partial I_\mathrm{U}}\frac{\partial I_\mathrm{U}}{\partial x_\mathrm{g}}\right)^2_{x_\mathrm{g}=\bar{x}_\mathrm{g}=p_2/2} + \left(\frac{\partial M}{\partial I_\mathrm{D}}\frac{\partial I_\mathrm{D}}{\partial x_\mathrm{g}}\right)^2_{x_\mathrm{g}=\bar{x}_\mathrm{g}=p_2}\right]\sigma^2_{x_\mathrm{g}}.$$

Using Eqs. (5), (7) , and (14), we obtain

$$\begin{aligned}\sigma^2_{M,\mathrm{me}} &= \frac{2\pi^2V^2\cos^2\varphi}{p_2^2}\sigma^2_{x_\mathrm{g}},\\ \sigma^2_{\theta,\mathrm{me}} &= \left[\left(\frac{\partial\theta}{\partial I_\mathrm{U}}\frac{\partial I_\mathrm{U}}{\partial x_\mathrm{g}}\right)^2_{x_\mathrm{g}=\bar{x}_\mathrm{g}=p_2/2} + \left(\frac{\partial\theta}{\partial I_\mathrm{P}}\frac{\partial I_\mathrm{P}}{\partial x_\mathrm{g}}\right)^2_{x_\mathrm{g}=\bar{x}_\mathrm{g}=3p_2/4}\right.\\ &\quad\left. + \left(\frac{\partial\theta}{\partial I_\mathrm{D}}\frac{\partial I_\mathrm{D}}{\partial x_\mathrm{g}}\right)^2_{x_\mathrm{g}=\bar{x}_\mathrm{g}=p_2}\right]\sigma^2_{x_\mathrm{g}}.\end{aligned} \tag{B1}$$

Using Eqs. (5)–(7), and (14), we have

$$\begin{aligned}\sigma^2_{\theta,\mathrm{me}} &= \frac{[\cos^2\varphi+2\sin^4\varphi]}{2D^2}\sigma^2_{x_\mathrm{g}},\\ \sigma^2_{\upsilon^2,\mathrm{me}} &= \left[\left(\frac{\partial\upsilon^2}{\partial I_\mathrm{U}}\frac{\partial I_\mathrm{U}}{\partial x_\mathrm{g}}\right)^2_{x_\mathrm{g}=\bar{x}_\mathrm{g}=p_2/2} + \left(\frac{\partial\upsilon^2}{\partial I_\mathrm{P}}\frac{\partial I_\mathrm{P}}{\partial x_\mathrm{g}}\right)^2_{x_\mathrm{g}=\bar{x}_\mathrm{g}=3p_2/4}\right.\\ &\quad\left. + \left(\frac{\partial\upsilon^2}{\partial I_\mathrm{D}}\frac{\partial I_\mathrm{D}}{\partial x_\mathrm{g}}\right)^2_{x_\mathrm{g}=\bar{x}_\mathrm{g}=p_2}\right]\sigma^2_{x_\mathrm{g}}.\end{aligned} \tag{B2}$$

Using Eqs. (5)–(7), and (14), we obtain

$$\sigma^2_{\upsilon^2,\mathrm{me}} = \frac{p_2^2}{2\pi^2D^4}\cos^2\varphi\left[3+V^2+2(V-\cos\varphi)\cos\varphi\right]\sigma^2_{x_\mathrm{g}}. \tag{B3}$$

References

[1] Fitzgerald R 2000 *Phys. Today* **53** 23
[2] Momose A and Fukuda J. 1995 *Med. Phys.* **22** 375
[3] Bonse U and Hart M 1965 *Appl. Phys. Lett.* **6** 155
[4] Momose A, Takeda T, Itai Y and Hirano K 1996 *Nat. Med.* **2** 473
[5] Davis T, Gao D, Gureyev T, Stevenson A and Wilkins S 1995 *Nature* **373** 595
[6] Chapman D, Thomlinson W, Johnston R E, Washburn D, Pisano E, Gmur N, Zhong Z, Menk R, Arfelli F and Sayers D 1997 *Phys. Med. Biol.* **42** 2015
[7] Zhu P P, Wang J Y, Yuan Q X, Huang W X, Shu H, Gao B, Hu T D and Wu Z Y 2005 *Appl. Phys. Lett.* **87** 264101
[8] Zhu P P, Yuan Q X, Huang W X, Wang J Y, Shu H, Chen B, Liu Y J, Li E and Wu Z Y 2006 *J. Phys. D: Appl. Phys.* **39** 4142
[9] Nugent K, Gureyev T, Cookson D, Paganin D and Barnea Z 1996 *Phys. Rev. Lett.* **77** 2961
[10] Wilkins S, Gureyev T, Gao D, Pogany A and Stevenson A 1996 *Nature* **384** 335
[11] Pfeiffer F, Weitkamp T, Bunk O and David C 2006 *Nat. Phys.* **2** 258
[12] Pfeiffer F, Bech M, Bunk O, Kraft P, Eikenberry E F, Bronnimann C H, Grunzweig C and David C 2008 *Nat. Mater.* **7** 134
[13] David C, Nöhammer B, Solak H H and Ziegler E 2002 *Appl. Phys. Lett.* **81** 3287
[14] Momose A, Kawamoto S, Koyama I, Hamaishi Y, Takai K and Suzuki Y 2003 *Jpn. J. Appl. Phys.* **42** L866
[15] Weitkamp T, David C, Bunk O, Bruder J, Cloetens P and Pfeiffer F 2008 *Eur. J. Radiol.* **68** S13
[16] Mcdonald S A, Marone F, Hintermuller C, Mikuljan G, David C, Pfeiffer F and Stampanoni M 2009 *J. Synchrotron Radiat.* **16** 562
[17] Herzen J, Donath T, Pfeiffer F, Bunk O, Padeste C, Beckmann F, Schreyer A and David C 2009 *Opt. Express* **17** 10010
[18] Donath T, Pfeiffer F, Bunk O, Grunzweig C, Hempel E, Popsecu S, Vock P and David C 2010 *Invest. Radiol.* **45** 445
[19] Stutman D, Beck T J, Carrino J A and Bingham C O 2011 *Phys. Med. Biol.* **56** 5697
[20] Weitkamp T, Diaz A, David C, Pfeiffer F, Stampanoni M, Cloetens P and Ziegler E 2005 *Opt. Express* **13** 6296
[21] Bech M, Jensen T H, Feidenhans'l R, Bunk O, David C and Pfeiffer F 2009 *Phys. Med. Biol.* **54** 2747
[22] Zhu P P, Zhang K, Wang Z L, Liu Y J, Liu X S, Wu Z Y, Mcdonald S A, Marone F and Stampanoni M 2010 *Proc. Natl. Acad. Sci. USA* **107** 13576
[23] Zanette I, Bech M, Pfeiffer F and Weitkamp T 2011 *Appl. Phys. Lett.* **98** 094101
[24] Zanette I, Bech M, Rack A, Duc G L, Tafforeau P, David C, Mohr J, Pfeiffer F and Weitkamp T 2012 *Proc. Natl. Acad. Sci. USA* **109** 10199
[25] Li P, Zhang K, Bao Y, Ren Y Q, Ju Z Q, Wang Y, He Q L, Zhu Z Z, Huang W X, Yuan Q X and Zhu P P 2016 *Opt. Express* **24** 5829
[26] Revol V, Kottler C, Kaufmann R, Straumann U and Urban C 2010 *Rev. Sci. Instrum.* **81** 073709
[27] Chen G H, Zambelli J, Li K, Bevins N and Qi Z H 2011 *Med. Phys.* **38** 584
[28] Weber T, Bartl P, Durst J, Haas W, Michel T, Ritter A and Anton G 2011 *Nucl. Instrum. Methods Phys. Res. Sect A- Accel. Spectrom Dect. Assoc. Equip.* **648** S273
[29] Wu Z, Wang Z L, Gao K, Wang D J, Wang S H, Chen J, Chen H, Zhang K, Zhu P P and Wu Z Y 2014 *J. Electron Spectrosc. Relat. Phenom.* **196** 75
[30] Bronshtein I N, Semendyayev K A, Musiol G and Muehlig H 2013 *Handbook of Mathematics* (New York: Springer Science & Business Media) p. 791
[31] Chou C Y, Anastasio M A, Brankov J G, Wernick M N, Brey E M, Jr D M C and Zhong Z 2007 *Phys. Med. Biol.* **52** 1923